J. Fluid Mech. (2022), *vol*. 943, A14, doi:10.1017/jfm.2022.432

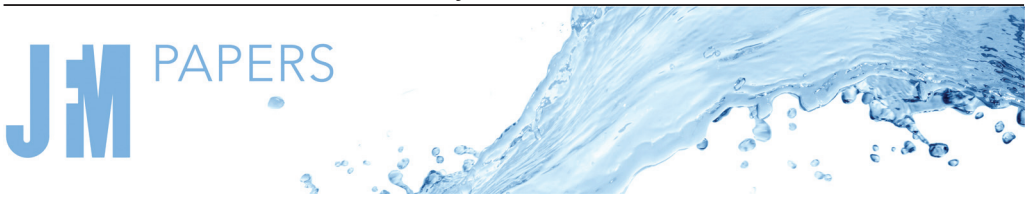

Wall-attached structures in a drag-reduced turbulent channel flow

Min Yoon[1,2] **and Hyung Jin Sung**[1],†

[1]Department of Mechanical Engineering, KAIST, 291 Daehak-ro, Yuseong-gu, Daejeon 34141, Korea

[2]Division of Mechanical Engineering, Korea Maritime and Ocean University, 727 Taejong-ro, Yeongdo-gu, Busan 49112, Korea

(Received 26 August 2021; revised 5 April 2022; accepted 11 May 2022)

We explore wall-attached structures in a drag-reduced turbulent channel flow with the Navier slip boundary condition. Three-dimensional coherent structures of the streamwise velocity fluctuations (u) are examined in an effort to assess the influence of wall-attached u structures on drag reduction. We extract the u clusters from the direct numerical simulation (DNS) data; the DNS data for the no-slip condition are included for comparison. The wall-attached structures, which are physically adhered to the wall, in the logarithmic region are self-similar with their height and contribute to the presence of logarithmic behaviour. The influence of the streamwise slip on wall-attached structures is limited up to the lower bound of the logarithmic region. Although wall-attached self-similar structures (WASS) slide at the wall, the formation and hierarchy of WASS are sustained. Weakened mean shear by the streamwise slip results in a diminution in the population density of wall-attached structures within the buffer layer, leading to sparse population of WASS. In contrast, the space occupied by WASS in the fluid domain increases. The streamwise slip induces long tails in the near-wall part of WASS, reminiscent of the footprints of large-scale motions. Both a decrease in the population density of WASS and a reduction in the density of skin friction of WASS are responsible for the overall drag reduction.

Key words: turbulent boundary layers, turbulence simulation

1. Introduction

Townsend (1976) posited that the main energy-containing motions in the logarithmic region are self-similar with respect to their height (l_y) and are attached to the wall. The attached-eddy hypothesis can be used to predict turbulence statistics through the construction of randomly superimposed attached eddies and can be rigorously applied to an inviscid fluid near the wall for high-Reynolds-number turbulent flows. Perry &

† Email address for correspondence: hjsung@kaist.ac.kr

Chong (1982) extended Townsend's attached-eddy hypothesis to establish the attached eddy model by using a hierarchy of self-similar vortex eddies with population densities that are inversely proportional to their height. Recently, Hwang & Sung (2018) extracted wall-attached structures from the direct numerical simulation (DNS) data for a turbulent boundary layer (TBL); they reported that wall-attached structures of the streamwise velocity fluctuations (u) with an inverse power-law distribution contribute to the presence of the logarithmic region and are physically anchored to the wall. The near-wall turbulence is dominantly influenced by the viscosity and is closely related to the skin-friction reduction in drag-reduced flows (Min & Kim 2004; Kim 2011). Hence, the mechanism of drag reduction can be explored by examining near-wall parts of wall-attached structures.

Many studies of wall-attached structures have now been conducted. In the logarithmic region, the turbulence statistics can be determined by performing the random superposition of self-similar attached eddies with various sizes,

$$\langle uu\rangle/u_\tau^2 = B_1 - A_1 \ln(y/\delta), \tag{1.1}$$

$$\langle ww\rangle/u_\tau^2 = B_2 - A_2 \ln(y/\delta), \tag{1.2}$$

$$\langle vv\rangle/u_\tau^2 = B_3, \tag{1.3}$$

where v and w are the wall-normal and spanwise velocity fluctuations, respectively, $\langle\cdot\rangle$ denotes ensemble- and time-averaged quantities, u_τ represents the friction velocity, A_1, A_2, B_1, B_2 and B_3 are constants, y is the wall-normal location and δ is the 99 % boundary layer thickness, channel half-height or pipe radius. Perry & Abell (1977) demonstrated the presence of a k_x^{-1} region in the streamwise spectra of u, where k_x is the streamwise wavenumber. Perry & Chong (1982) applied geometrically self-similar hierarchies to attached eddies in their model. Perry, Henbest & Chong (1986) introduced a weighting for δ-height attached eddies in the population density to account for the velocity defect law and low-wavenumber energy in the spectra. Research into wall-attached eddies and their models has been summarized in a recent review by Marusic & Monty (2019).

Several studies of high-Reynolds-number wall-bounded turbulence ($Re_\tau > O(10^{3-4})$) have been performed, and their results support Townsend's attached-eddy hypothesis. Here, $Re_\tau (= u_\tau\delta/\nu)$ is the friction Reynolds number, where ν is the kinematic viscosity. For instance, the logarithmic variation was observed in the streamwise Reynolds stress (Hutchins *et al.* 2009; Hultmark *et al.* 2012; Hutchins *et al.* 2012; Lee & Moser 2015). A k_x^{-1} region has been reported in the energy spectra of u (Nickels *et al.* 2005; Ahn *et al.* 2015; Lee & Moser 2015). In addition, coherent wall-attached structures have been extracted from instantaneous flow fields (del Álamo *et al.* 2006; Flores, Jiménez & del Álamo 2007; Lozano-Durán, Flores & Jiménez 2012; Lozano-Durán & Jiménez 2014; Dong *et al.* 2017; Maciel, Gungor & Simens 2017; Maciel, Simens & Gungor 2017; Hwang & Sung 2018; Osawa & Jiménez 2018; Han *et al.* 2019; Hwang & Sung 2019; Lozano-Durán & Bae 2019; Yang, Hwang & Sung 2019; Hwang, Lee & Sung 2020; Yoon *et al.* 2020; Bae & Lee 2021; Wang *et al.* 2021). The identified clusters can be classified as either wall-attached or wall-detached structures according to their minimum distance from the wall. Wall-attached coherent structures are self-similar with their height and make dominant contributions to the turbulence statistics in the logarithmic region.

A strong shear layer is formed near the wall, which results in high skin friction in wall-bounded turbulence. The Navier slip boundary condition (Navier 1823) is one of several kinds to mimic drag-reduced turbulent flows in the streamwise direction (Min & Kim 2004; Yoon *et al.* 2016*b*; Ryu *et al.* 2019), assuming that a spanwise slip is relatively small. Chung, Monty & Ooi (2014) reported that the first- and second-order

turbulence statistics in the region of $y > 30\nu/u_\tau$ in a turbulent channel flow with slip velocities parallel to the wall are identical to those of the no-slip counterpart, which supports Townsend's outer-layer similarity hypothesis (Townsend 1976). Lozano-Durán & Bae (2019) extracted intense sweep and ejection motions in a turbulent channel flow with slip velocities in all directions. They showed that the streamwise and spanwise length scales of wall-attached sweeps and ejections with heights greater than $100\nu/u_\tau$ coincide with those at the no-slip wall. Although many studies of turbulence statistics and structures in drag-reduced flows have been performed, not much attention has been paid to wall-attached structures, especially in the vicinity of the wall. Given that wall-attached structures are the main energy-containing motions in the logarithmic region and physically anchored to the wall, it is essential to establish the role of the roots of wall-attached structures in the frictional drag to understand the mechanism of drag reduction.

The objective of the present study was to explore the role of wall-attached u structures in drag reduction, especially focused on their near-wall part. To this end, the DNS data of a turbulent channel flow ($Re_b = 10\,333$) with the Navier slip were used. Here, $Re_b (= U_b\delta/\nu)$ is the Reynolds number based on the bulk velocity (U_b). For comparison, the DNS data for the no-slip condition at the same Re_b were included in the present study. This paper has six sections. The numerical procedure for DNS is presented in § 2. We extract three-dimensional (3-D) u clusters from the instantaneous flow fields, classified into wall-attached and wall-detached structures according to the minimum distance from the wall (§ 3.1). In § 3.2, the influences of the streamwise slip on wall-attached structures are analysed. The logarithmic behaviour and hierarchical feature of wall-attached structures are not influenced by the streamwise slip. We decompose wall-attached structures into three groups according to their self-similarity and wall-normal location. The structural features of the near-wall part of wall-attached self-similar structures are scrutinized by using conditional two-point correlations (§ 4.1). The turbulence statistics carried by the near-wall part of wall-attached self-similar structures are examined in § 4.2. Contributions of the wall-attached structures (§ 5.1) and near-wall part of self-similar structures (§ 5.2) to drag reduction are explored. The near-wall part of wall-attached self-similar structures encompasses the main energy-containing motions near the wall and makes a dominant contribution to the frictional drag. Our conclusions are provided in § 6.

2. Numerical details

In the present study, the DNS data for turbulent channel flows with the Navier slip and no-slip boundary conditions of Yoon *et al.* (2016*b*) were used. The Navier−Stokes equations and continuity equation for an incompressible flow were discretized by using the fractional step method (Kim, Baek & Sung 2002). The bulk Reynolds number (Re_b) is 10 333. The periodic boundary condition was used in the streamwise and spanwise directions. The sizes of the computational domain were selected so as to fully resolve the streamwise-long motions; the streamwise size was more than 30 times longer than the channel half-height. The time steps in the wall units were 0.0426 and 0.0645 for the slip and no-slip cases, respectively. The averaging time was $330\delta/U_b$. The characteristics of the computational domain are summarized in table 1, where x and z are the streamwise and spanwise directions, respectively, and the superscript '+' denotes quantities normalized by the wall units of each boundary condition.

The Navier slip boundary condition (Navier 1823) was applied in the streamwise direction, i.e. $\tilde{u}_S = L_S(\mathrm{d}\tilde{u}/\mathrm{d}y)|_{wall}$, where $\tilde{u}_S$ is the slip velocity, L_S is the slip length and $\tilde{u}$ is the streamwise velocity. Here, $\tilde{u}$ $(= U + u)$ can be decomposed into the streamwise mean velocity (U) and its fluctuations (u). Figure 1 shows the relationships between the

	L_x/δ	L_z/δ	N_x	N_y	N_z	Δx^+	Δz^+	Δy^+_{min}	Δy^+_{max}	Re_τ
Slip	10π	3π	2497	401	1249	5.92	3.55	0.08	5.96	469
No-slip	10π	3π	2497	401	1249	7.27	4.36	0.10	7.32	577

Table 1. Parameters of the computational domain and friction Reynolds number (Re_τ). Here, L_i and N_i are the domain size and the number of grids in each direction, respectively, and Δy^+_{min} and Δy^+_{max} are the resolutions of the first grid from the wall and the grid at the channel half-height, respectively.

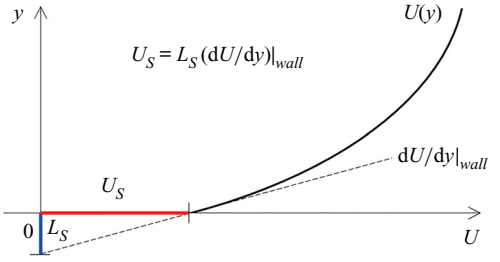

Figure 1. Schematic diagram of the streamwise mean velocity (U), where U_S and L_S are the mean slip velocity and slip length, respectively.

streamwise mean velocity, the mean slip velocity (U_S) and L_S. The slip length is fixed at $L_S = 0.01\delta$ to give a drag reduction rate of 34 % for the channel flow with the no-slip condition (Fukagata, Kasagi & Koumoutsakos 2006). Consequently, the friction Reynolds numbers (Re_τ) for the slip and no-slip cases are 469 and 577, respectively. Details of the numerical procedure and its validation can be found in Yoon *et al.* (2016*b*).

2.1. *Turbulence statistics*

Figure 2 shows the turbulence statistics of turbulent channel flows with slip and no-slip conditions. The quantities are normalized by the wall units of each case. The magnitude of streamwise mean velocity (U^+) is larger than that of the no-slip case due to the streamwise slip (figure 2*a*). The dashed line in figure 2(*a*) represents the mean velocity relative to the wall ($U^+ - U^+_S$) for the slip case, which coincides with the profile of U^+ for the no-slip case. The mean shear in the wall units ($\mathrm{d}U^+/\mathrm{d}y^+$) is insensitive to the streamwise slip. The streamwise slip induces a virtual origin in U^+ at $y^+ = -L^+_S$, leading to the upward shift of U^+ as $\Delta U^+ = U^+_S = L^+_S$ in the entire region (García-Mayoral, Gómez-de-Segura & Fairhall 2019). The streamwise turbulence intensity (u^+_{rms}) is amplified with respect to that of the no-slip case below $y^+ = 10$, especially very close to the wall (figure 2*c*), due to the streamwise slip. A virtual origin for turbulence is absent due to the combined influences of wall-normal and spanwise slip lengths (Ibrahim *et al.* 2021), showing almost the same inner peaks of u^+_{rms} (Kim, Moin & Moser 1987). In contrast, a profile of Reynolds shear stress ($\langle -uv \rangle^+$) is well matched with that for the no-slip case in the inner region as a result of an impermeable condition at the wall. For outer scaling, the profiles of $U^+_c - U^+$ (figure 2*b*), u^+_{rms} and $\langle -uv \rangle^+$ (figure 2*d*) for both cases collapse well in the outer region, supporting Townsend's outer-layer similarity hypothesis and in agreement with the results of Flores & Jiménez (2006) and Chung *et al.* (2014). Here, U_c is the mean velocity at the channel centre.

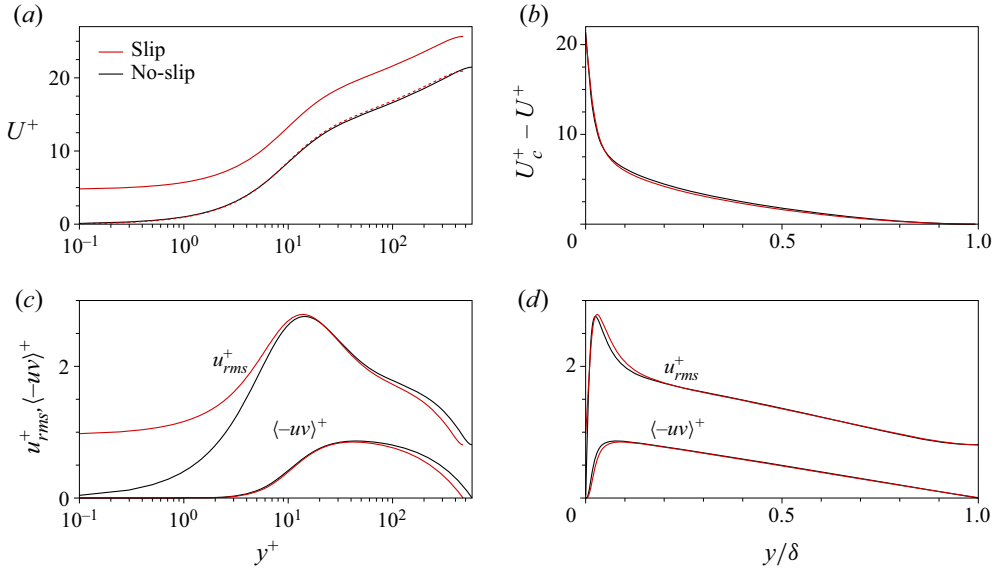

Figure 2. Profiles of (*a*) mean velocity (U^+) and (*b*) defect form ($U_c^+ - U^+$) of mean velocity, where U_c is the mean velocity at the channel centre. A dashed line in panel (*a*) represents mean velocity relative to wall ($U^+ - U_S^+$) for the slip case. Profiles of streamwise turbulence intensity (u_{rms}^+) and Reynolds shear stress ($\langle -uv \rangle^+$) for (*c*) inner scaling and (*d*) outer scaling.

3. Wall-attached structures

3.1. *Identification of coherent structures*

The 3-D u clusters in instantaneous flow fields can be defined as the groups of connected points satisfying $u(\boldsymbol{x}, t) \geq \alpha u_{rms}(y)$ and $u(\boldsymbol{x}, t) \leq -\alpha u_{rms}(y)$. Here, α is the threshold, which is selected from the percolation diagram in figure 3(*a*), and $\boldsymbol{x}$ and t represent the spatial vector and time, respectively. The total number (N) and total volume (V) of u clusters at a given α are normalized by the maximum N (N_{max}) and maximum V (V_{max}), respectively. As α decreases, new clusters appear or some adjacent clusters merge. The peak in N/N_{max} at $\alpha = 1.6$ results from the tradeoff between these two influences; the former is dominant for $\alpha > 1.6$ and *vice versa*. In addition, V/V_{max} increases as α decreases with strong variation in the region of $1.4 < \alpha < 1.8$, where the percolation transition occurs. Hence, we chose $\alpha = 1.6$ in the present study.

Based on this condition, each u cluster can be detected by using the connectivity of six-orthogonal grids at a given node in Cartesian coordinates (Moisy & Jiménez 2004; del Álamo *et al.* 2006; Lozano-Durán *et al.* 2012; Hwang & Sung 2018; Lozano-Durán & Bae 2019; Hwang *et al.* 2020; Yoon *et al.* 2020). As a result, the spatial information for each u cluster can be obtained. The u clusters with volumes less than 30^3 wall units are discarded to avoid grid resolution (del Álamo *et al.* 2006). Figure 3(*b*) shows the population density (n^*) of all the identified u clusters as functions of y_{max} and y_{min}, which are the maximum and minimum distances from the wall, respectively. Here, n^* is defined as the number of u clusters (n) per unit wall-parallel area ($A_{xz} = L_x L_z$), i.e. $n^* = n(y_{max}, y_{min})/(mA_{xz})$, where m is the number of snapshots ($m = 1164$ for the slip case and $m = 1144$ for the no-slip case). Two distinct groups are evident at $y_{min}^+ \approx 0$ and $y_{min}^+ > 0$, where the former are wall-attached structures and the latter are wall-detached structures (Hwang & Sung 2018; Yoon *et al.* 2020).

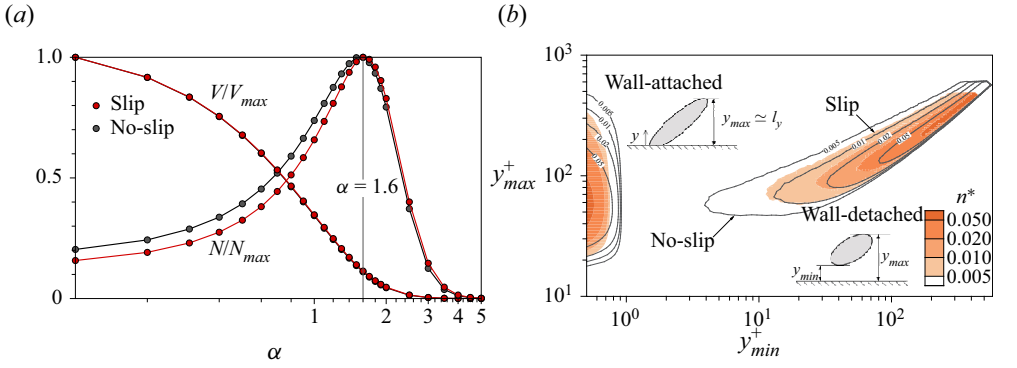

Figure 3. (*a*) Percolation diagram for the detected *u* clusters. Variations with α in the total volume (V) and total number (N) of clusters. (*b*) Number of *u* clusters per unit wall-parallel area (n^*) with respect to y^+_{min} and y^+_{max}.

The 3-D iso-surfaces of *u* of wall-attached and wall-detached structures are shown in figure 4(*a*) for the slip case and in figure 4(*b*) for the no-slip case. Blue and red correspond to negative *u* and positive *u*, respectively. The characteristic length scales of each *u* cluster can be defined in terms of the dimensions of the box circumscribing the object. The inset in figure 4(*a*) shows a wall-attached structure and its length scales, i.e. l_x, l_z and l_y, which are the streamwise and spanwise sizes and the height, respectively. As can be seen in figure 4, the wall-attached *u* structures are coherent in the streamwise direction and aligned side by side in the spanwise direction. At first sight, those for the slip case appear similar respectively to those for the no-slip case. However, upon closer inspection, differences in terms of the population density of the wall-attached structures are observed. The wall-attached structures are sparsely distributed for the slip case. The streamwise slip induces streamwise velocities at the wall (figure 2*a*) and enhances the magnitude of u^+_{rms} near the wall (figure 2*c*). We can observe sparse wall-attached structures in an instantaneous flow field despite the presence of slip at the wall. The wall-detached structures are less coherent than the wall-attached structures and are randomly distributed in the domain.

3.2. *Influences of streamwise slip on wall-attached structures*

Figure 5 shows the joint probability density functions (JPDF) of l^+_x and l^+_z with respect to l^+_y, which is the height of wall-attached structures ($l_y = y_{max}$, $l^+_y \approx y^+$ because of $y_{min} \approx 0$). Colour and line contours apply to the slip and no-slip cases, respectively. Circles correspond to the mean lengths for the slip (red) and no-slip (black) cases.

As shown in figure 5(*a*), the mean $l^+_x(\langle l^+_x \rangle)$ is proportional to l^+_y with the power of 0.74 (Hwang & Sung 2018) in the region of $l^+_y \geq 70 \approx 3Re^{0.5}_\tau$, whereas not proportional to $l^+_y (l^+_y < 70)$. Here, $3Re^{0.5}_\tau$ is the lower limit of the logarithmic region (Marusic *et al.* 2013; Hwang & Sung 2019), which accords with approximately $70\nu/u_\tau$ at the present Reynolds number ($Re_\tau \approx 500$). In addition, there is a linear relationship between the mean $l^+_z(\langle l^+_z \rangle)$ and $l^+_y (l^+_y \geq 70)$ (figure 5*b*), which shows that the spanwise size of wall-attached *u* structures is proportional to the distance from the wall (Tomkins & Adrian 2003; del Álamo *et al.* 2006; Hwang 2015). In particular, the JPDF of l^+_x and l^+_z with l^+_y for both cases coincide in the entire l^+_y region, especially $l^+_y \geq 70$, in agreement with the results

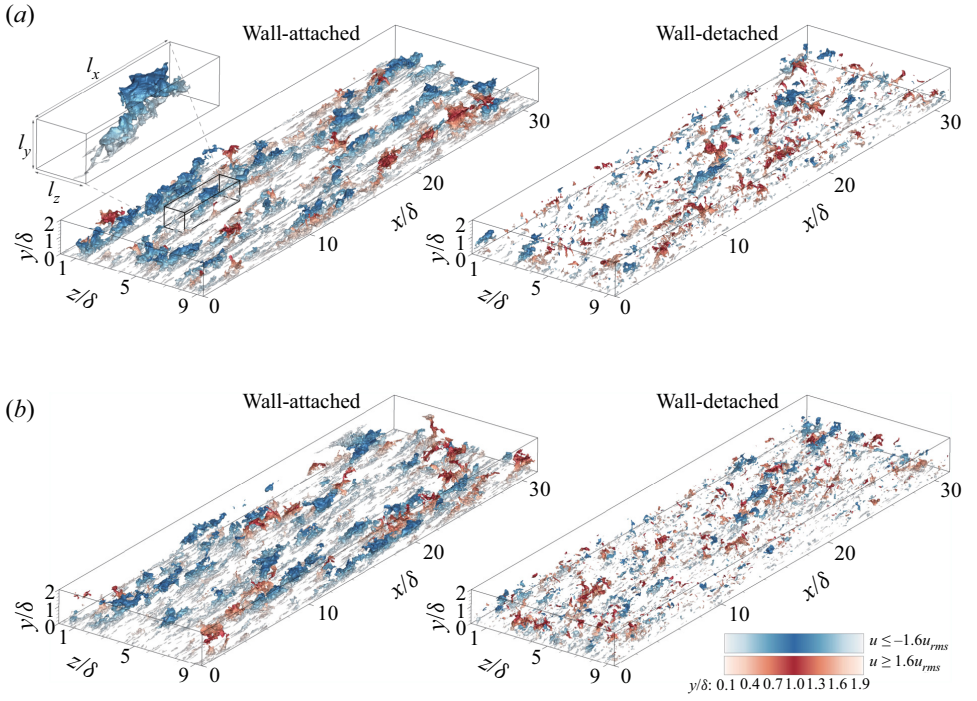

Figure 4. 3-D iso-surfaces of the wall-attached and wall-detached u structures in an instantaneous flow field for (a) the slip case and (b) the no-slip case.

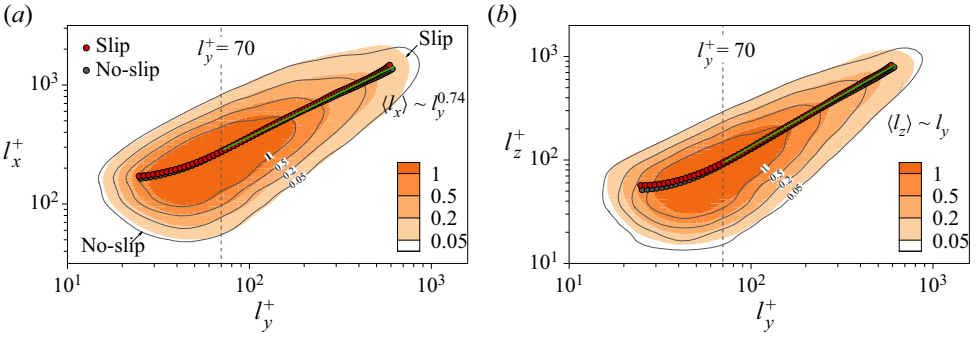

Figure 5. Contours of JPDF of (a) l_x^+ and l_y^+ and of (b) l_z^+ and l_y^+ of wall-attached u structures. The circles are the mean lengths. The green lines in panels (a) and (b) are $\langle l_x \rangle \sim l_y^{0.74}$ and $\langle l_z \rangle \sim l_y$, respectively.

of Lozano-Durán & Bae (2019). Accordingly, we divide wall-attached structures into non-self-similar ($l_y^+ < 70$) and self-similar ($l_y^+ \geq 70$) structures.

The population density (n_a^*) of wall-attached structures with respect to l_y^+ is shown in figure 6(a). Here, n_a is the number of wall-attached structures as a function of their height l_y, and the population density (n_a^*) of wall-attached structures is defined as n_a per unit wall-parallel area, i.e. $n_a^* = n_a/(mA_{xz})$. The magnitude of n_a^* is smaller than that for the no-slip case in the entire region. The wall-attached structures with the height of $l_y^+ = O(10)$ are related to near-wall streaks. As shown in figure 2(a), the mean shear is preserved near the wall for the slip case, sustaining turbulence via the formation process of streaky

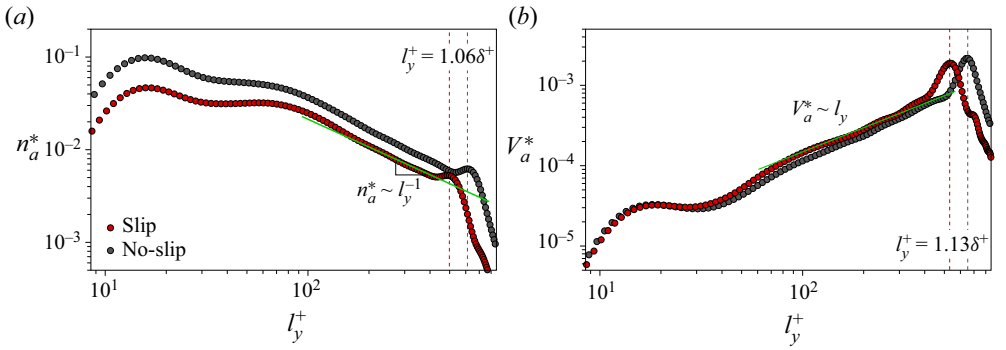

Figure 6. (*a*) Population density (n_a^*) and (*b*) volumes of wall-attached structures per unit domain volume (V_a^*) as a function of l_y^+. Green lines denote an inverse power-law distribution of n_a^* in panel (*a*) and linear variation in V_a^* in panel (*b*). Dashed lines in panels (*a*) and (*b*) represent $l_y^+ = 1.06\delta^+$ and $l_y^+ = 1.13\delta^+$, respectively.

structures (Hamilton, Kim & Waleffe 1995; Waleffe 1997). The streamwise slip attenuates streamwise vortices near the wall, creating streaks sparsely (Min & Kim 2004; Kim 2011). The lack of streamwise vortices leads to reduced populations of wall-attached structures near the wall.

The magnitude of n_a^* is inversely proportional to l_y^+ in the region of $250 < l_y^+ < 400$ for both cases, reminiscent of the distribution of hierarchy length scales of attached eddies (Perry & Chong 1982). The inverse power-law dependence arises within the region of $l_y^+ = 0.3\delta^+ - 0.6\delta^+$ for zero-pressure-gradient TBL at $Re_\tau \approx 1000$ (Hwang & Sung 2018) and turbulent pipe flows at $Re_\tau \approx 1000$ and 3000 (Hwang & Sung 2019). The streamwise slip induces a decrease in the population density of wall-attached structures, but the inverse power law is still valid. The no-slip boundary condition is not indispensable to form hierarchical distributions of wall-attached structures. In addition, a peak in n_a^* arises at $l_y^+ = 1.06\delta^+$ for both cases, which results from the large population of wall-attached δ-height structures (Perry *et al.* 1986).

In contrast to the variation in n_a^*, the magnitude of V_a^* increases with increasing l_y^+ up to $l_y^+ \approx \delta^+$ (figure 6*b*). Here, V_a^* is defined as the volume of wall-attached structures per unit domain volume, i.e. $V_a^* = V_a/(mA_{xz}\delta)$, where $A_{xz}\delta$ is the domain volume. The profiles of V_a^* for both cases collapse well below $l_y^+ = 30$. The magnitude of V_a^* is even larger than that for the no-slip case in the region of $l_y^+ = 30 - 550$, whereas the number of wall-attached structures is smaller than that for the no-slip case (figure 6*a*). A peak in V_a^* arises at $l_y^+ = 1.13\delta^+$ for both cases; this trend is the same as that in n_a^*.

Figure 7 shows wall-normal profiles of streamwise Reynolds stresses ($\langle uu\rangle_a^{*+}$) carried by the wall-attached structures with the height of $l_y^+ = 300$ and $1.06\delta^+$,

$$\langle uu\rangle_a^*(y, l_y) = \left\langle S_a(y, l_y)^{-1} \int_{S_a} u(\boldsymbol{x})u(\boldsymbol{x})\,\mathrm{d}x\,\mathrm{d}z \right\rangle, \tag{3.1}$$

where S_a is the wall-parallel area of wall-attached structures as functions of y and l_y. As shown in figure 7(*a*), the magnitude of $\langle uu\rangle_a^{*+}$ for $l_y^+ = 300$ is logarithmically proportional to y^+ ($\langle uu\rangle_a^{*+} \sim \ln y^+$) in the region of $100 < y^+ < 220$ (Perry & Chong 1982). Although the present Reynolds number is relatively low ($Re_\tau \approx 500$), the logarithmic variation is evident in $\langle uu\rangle_a^{*+}$ reconstructed from the wall-attached structures (Hwang & Sung 2018; Hwang *et al.* 2020; Yoon *et al.* 2020). Wall-attached δ-height structures are not self-similar with their height, but contaminate the logarithmic variation in the streamwise Reynolds

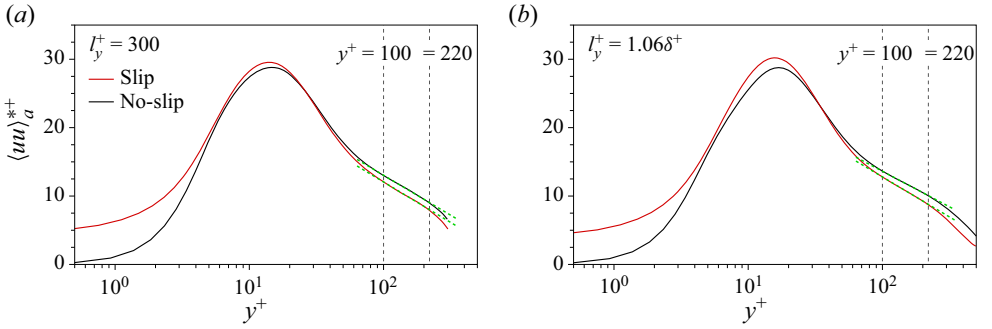

Figure 7. Streamwise Reynolds stresses ($\langle uu \rangle_a^+$) reconstructed by wall-attached structures with the height of (*a*) $l_y^+ = 300$ and (*b*) $l_y^+ = 1.06\delta^+$. Green dashed lines in panel (*a*) indicate the best fits in the region of $100 < y^+ < 220$: $\langle uu \rangle_a^{*+} = 35.73 - 5.14 \ln y^+$ for the slip case and $\langle uu \rangle_a^{*+} = 36.44 - 5.08 \ln y^+$ for the no-slip case, and those in panel (*b*) are for $\langle uu \rangle_a^{*+} = 36.24 - 5.09 \ln y^+$ (slip) and $\langle uu \rangle_a^{*+} = 34.44 - 4.52 \ln y^+$ (no-slip). Two vertical dashed lines represent $y^+ = 100$ and $y^+ = 220$.

stress (Hwang *et al.* 2020; Yoon *et al.* 2020). Wall-attached δ-height structures are self-similar with l_y (figure 5). The profiles of $\langle uu \rangle_a^{*+}$ for $l_y^+ = 1.06\delta^+$ are similar to those for $l_y^+ = 300$, and the logarithmic variation is still valid in the region of $l_y^+ = 100 - 220$ (figure 7*b*). The logarithmic behaviour of wall-attached structures is sustained regardless of the streamwise slip at the wall.

4. Near-wall part of wall-attached self-similar structures

Townsend's attached-eddy hypothesis (Townsend 1976) is useful for the prediction of turbulence statistics in the logarithmic region; coherent structures are constructed through the superposition of attached self-similar eddies. However, careful attention must be paid to the use of attached-eddy models, since Townsend's attached-eddy hypothesis strictly only applies to high-Reynolds-number wall-bounded flows, which are inviscid near the wall. To limit the influence of viscosity on wall-attached structures, the majority of studies have focused on wall-attached structures above the logarithmic region (del Álamo *et al.* 2006; Lozano-Durán *et al.* 2012; Hwang & Sung 2018; Yoon *et al.* 2020). Hwang & Sung (2018) observed an inverse power law in the population density ($290 < l_y^+ < 550$) of wall-attached structures that is responsible for the logarithmic variation in the streamwise Reynolds stress ($3Re_\tau^{0.5} < y^+ < 0.18\delta^+$). Wall-attached structures with $3Re_\tau^{0.5} \leq l_y^+ \leq 0.6\delta^+$ are self-similar with their height (Hwang *et al.* 2020).

4.1. *Structural features*

The characteristics of wall-attached structures can be divided into buffer-layer ($l_y^+ < 70 \approx 3Re_\tau^{0.5}$) and self-similar ($l_y^+ \geq 70$) structures. As shown in figure 5, the upper part ($y^+ \geq 70$) of WASS ($l_y^+ \geq 70$) is responsible for the logarithmic behaviour (figure 7*b*). The near-wall part ($y^+ < 70$) of WASS ($l_y^+ \geq 70$) contributes to geometrical self-similarity (figure 5). The wall-attached structures can be decomposed into u_{nws}, u_{uws} and u_{wb}, which

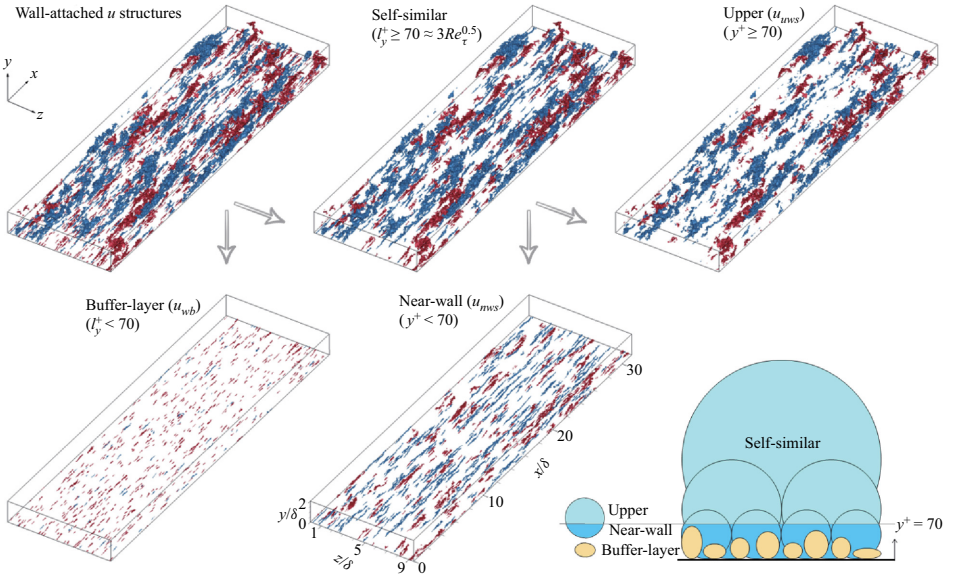

Figure 8. 3-D iso-surfaces of u wall-attached structures: self-similar ($l_y^+ \geq 70 \approx 3Re_\tau^{0.5}$); the upper part ($u_{uws}$) ($l_y^+ \geq 70$ and $y^+ \geq 70$) and near-wall part (u_{nws}) ($l_y^+ \geq 70$ and $y^+ < 70$) and buffer-layer (u_{wb})($l_y^+ < 70$). Red and blue correspond to positive u and negative u, respectively.

are defined as

$$u_{nws}(\boldsymbol{x}) = \begin{cases} u & \text{if } |u| \geq 1.6u_{rms},\ y^+_{min} \approx 0,\ y^+_{max} \geq 70,\ y^+ < 70, \\ 0 & \text{otherwise,} \end{cases} \tag{4.1a}$$

$$u_{uws}(\boldsymbol{x}) = \begin{cases} u & \text{if } |u| \geq 1.6u_{rms},\ y^+_{min} \approx 0,\ y^+_{max} \geq 70,\ y^+ \geq 70, \\ 0 & \text{otherwise,} \end{cases} \tag{4.1b}$$

$$u_{wb}(\boldsymbol{x}) = \begin{cases} u & \text{if } |u| \geq 1.6u_{rms},\ y^+_{min} \approx 0,\ y^+_{max} < 70, \\ 0 & \text{otherwise.} \end{cases} \tag{4.1c}$$

Here, the subscripts '*nws*', '*uws*' and '*wb*' represent the near-wall part of WASS, upper part of WASS and wall-attached buffer-layer structures (WABS), respectively. From now on, we focus on the near-wall part of WASS, in which the viscosity effect is dominant.

Figure 8 illustrates 3-D iso-surfaces of u wall-attached structures for the no-slip case in an instantaneous flow field. Red and blue correspond to positive u and negative u, respectively. A schematic diagram in the inset of figure 9 helps to understand the decomposition of wall-attached structures: upper-part of self-similar, near-wall part of self-similar and buffer layer. Note that both u_{nws} and u_{wb} are located in the region of $y^+ < 70$. The near-wall part of WASS is more coherent than the WABS. In addition, the near-wall part of WASS ($y^+ < 70$) is easily observed in an instantaneous flow field, interpreted as the footprints of large-scale motions (Hutchins & Marusic 2007; Hwang *et al.* 2016).

To investigate sizes of the near-wall part of WASS statistically, conditional two-point correlations of u_{nws} are examined at the reference wall-normal location $y^+_{ref} = 14.5$, where the inner peak arises in u^+_{rms} (figure 2*c*). The two-point correlations of u_{nws} and u_{wb} are

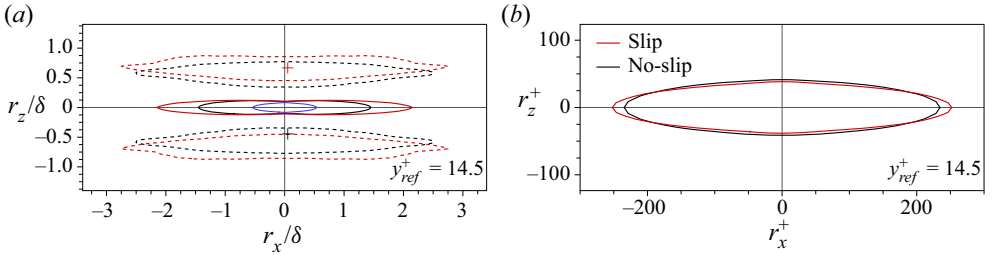

Figure 9. Two-point correlations of (*a*) u_{nws} and (*b*) u_{wb}. The reference wall-normal location is $y^+_{ref} = 14.5$. Solid lines represent 5 % of the maximum of positive correlations, and dashed lines denote 50 % of the minimum of negative correlations. Cross symbols indicate spanwise centres of negative correlations. The blue line in panel (*a*) accords with $R[u_{wb}, u_{wb}]$ for the slip case in panel (*b*).

defined as

$$R[u_{nws}, u_{nws}](r_x, y, r_z, y_{ref}) = \frac{\langle u_{nws}(x, y_{ref}, z) u_{nws}(x + r_x, y, z + r_z)\rangle}{u_{nws,\,rms}(y_{ref}) u_{nws,\,rms}(y)}, \tag{4.2a}$$

$$R[u_{wb}, u_{wb}](r_x, y, r_z, y_{ref}) = \frac{\langle u_{wb}(x, y_{ref}, z) u_{wb}(x + r_x, y, z + r_z)\rangle}{u_{wb,\,rms}(y_{ref}) u_{wb,\,rms}(y)}, \tag{4.2b}$$

where $u_{nws,rms}$ and $u_{wb,rms}$ are the root-mean-square quantities of u_{nws} and u_{wb}, respectively. For comparison, the two-point correlation of u_{wb} is included.

Wall-parallel views of $R[u_{nws}, u_{nws}]$ are shown in figure 9(*a*), where solid and dashed lines denote 5 % of the maximum of positive $R[u_{nws}, u_{nws}]$ and 50 % of the minimum of negative $R[u_{nws}, u_{nws}]$, respectively. The positive $R[u_{nws}, u_{nws}]$ are extended to approximately 4.3δ in the streamwise direction, which is similar to streamwise lengths of the footprints of large-scale motions at the same location of $y^+_{ref} \approx 14.5$ (Lee & Sung 2013; Hwang *et al.* 2016; Yoon *et al.* 2016*b*; Hwang & Sung 2017). In addition, the scaling of negative $R[u_{nws}, u_{nws}]$ with δ indicates that the near-wall part of WASS is aligned side by side along the spanwise direction. The distance to the centre (cross symbol) of negative $R[u_{nws}, u_{nws}]$ at $r_x = 0$ is 0.6δ, which is 20 % larger than that for the no-slip case. This result represents that the near-wall part of WASS is more sparsely distributed than those for the no-slip case (figure 4).

Figure 9(*b*) shows line contours of $R[u_{wb}, u_{wb}]$ in the x–z plane. Compared to $R[u_{nws}, u_{nws}]$, the negative $R[u_{wb}, u_{wb}]$ is not observed, representing that the WABS are not influenced by adjacent other WABS. This is consistent with the observations in figure 8, where iso-surfaces of u_{wb} are more sparsely populated than those of u_{nws}. The line contour of $R[u_{wb}, u_{wb}]$ is transversely away from the reference centre ($r_x = 0$ and $r_z = 0$) by $85\nu/u_\tau$, implying that the WABS are closely related to the near-wall streaks (Kline *et al.* 1967). The streamwise extension of positive $R[u_{wb}, u_{wb}]$ is $500\nu/u_\tau$ at $r_z = 0$, which is 7.7 % longer than that for the no-slip case. The blue contour in figure 9(*a*) represents $R[u_{wb}, u_{wb}]$ for the slip case, indicating that the WABS are much shorter in the streamwise direction than the near-wall part of WASS.

To further examine geometrical features of the near-wall part of WASS, two-point correlations of u_a ($R[u_a, u_a]$) at a given l_y are performed at $y^+_{ref} = 14.5$. The conditional field (u_a) and two-point correlation of u_a are defined as

$$u_a(\boldsymbol{x}, l_y) = \begin{cases} u & \text{if } |u| \geq 1.6 u_{rms},\ y^+_{min} \approx 0, \\ 0 & \text{otherwise,} \end{cases} \tag{4.3}$$

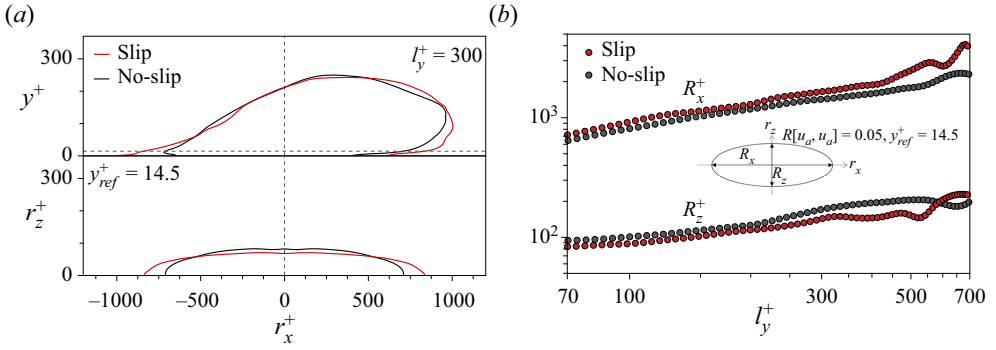

Figure 10. (*a*) Two-point correlations of u_a for $l_y^+ = 300$ in the x–y and x–z planes. The reference wall-normal location is $y_{ref}^+ = 14.5$. Line contours are $R[u_a, u_a] = 0.05$. (*b*) Streamwise and spanwise characteristic lengths (R_x^+ and R_z^+) of the near-wall part of WASS at $y_{ref}^+ = 14.5$ with respect to l_y^+.

$$R[u_a, u_a](r_x, y, r_z, y_{ref}, l_y) = \frac{\langle u_a(x, y_{ref}, z, l_y) u_a(x + r_x, y, z + r_z, l_y)\rangle}{u_{a,\,rms}(y_{ref}, l_y) u_{a,\,rms}(y, l_y)}, \tag{4.4}$$

where $u_{a,rms}$ is the root-mean-square quantity of u_a. Figure 10(*a*) shows the x–z plane (at $y^+ = y_{ref}^+$) and x–y plane (at $r_z^+ = 0$) views of $R[u_a, u_a]$ for $l_y^+ = 300$. The wall-attached structures with the height of $l_y^+ = 300$ are more stretched in both upstream and downstream directions than those for the no-slip case. These observations support that weakened wall-shear stress due to the streamwise slip results in a long extension of wall-attached structures to the wall (Chung *et al.* 2014).

Figure 10(*b*) shows characteristic length scales of the near-wall part of WASS at $y_{ref}^+ = 14.5$. Their streamwise and spanwise lengths (R_x and R_z) can be defined in terms of the difference between the streamwise and spanwise displacements at $R[u_a, u_a](r_x^+, y^+ = y_{ref}^+, r_z^+ = 0) = 0.05$ and $R[u_a, u_a](r_x^+ = 0, y^+ = y_{ref}^+, r_z^+) = 0.05$, respectively. The magnitude of R_x^+ and R_z^+ gradually increases for both cases with the increase in l_y^+. Interestingly, streamwise lengths of the near-wall part of WASS are longer than those for the no-slip case, and *vice versa* for the spanwise lengths up to $l_y^+ = 600$. The magnitude of R_x^+ is larger than $1\delta^+$, and is thus related to the footprints of large-scale motions (Hutchins & Marusic 2007). The magnitude of R_x^+ is approximately 1.3 times larger than that for the no-slip case up to $l_y^+ = 400$, over which the difference in R_x^+ between two cases becomes larger. Although sizes of WASS are independent of the streamwise slip (figure 5), their roots are stretched and compressed in the streamwise and spanwise directions, respectively.

4.2. *Conditional statistics*

We investigate the turbulence statistics of the near-wall part of WASS along the wall-normal location. The turbulence statistics for the near-wall part of WASS can be conditionally averaged based on conditional fields, where velocity and vorticity fluctuations are obtained using equations similar to (4.1*a*). Conditionally averaged quantities are used to assess contributions of the near-wall part of WASS to the turbulence statistics in the region of $y^+ < 70$.

Figure 11 introduces wall-normal profiles of conditional averages for the near-wall part of WASS. Profiles of A_{nws}/A_{xz} (figure 11*a*) represent wall-parallel areas occupied by the

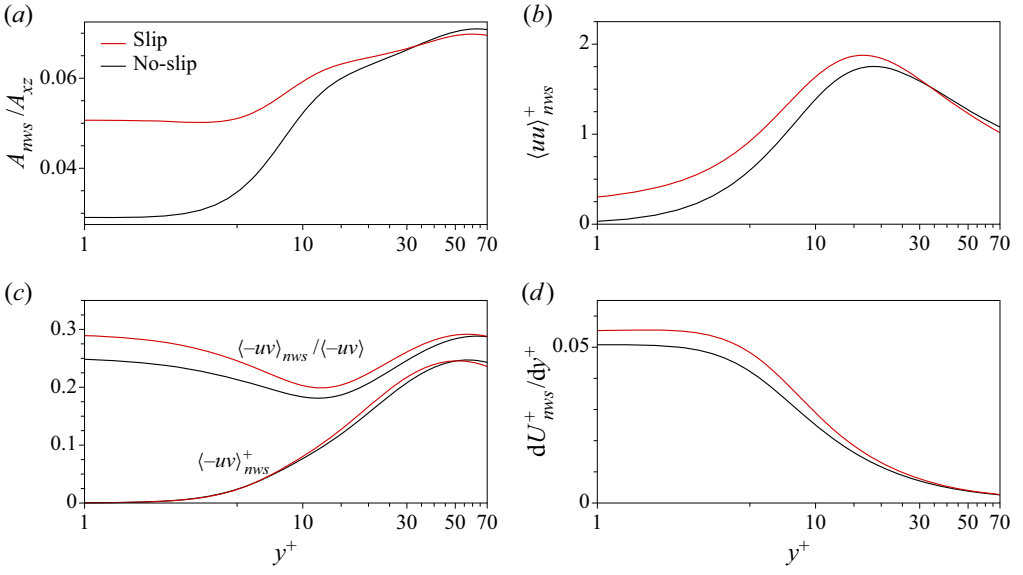

Figure 11. Conditionally averaged turbulence statistics of the near-wall part of WASS: wall-normal profiles of (*a*) A_{nws}/A_{xz}, (*b*) $\langle uu\rangle^+_{nws}$, (*c*) $\langle -uv\rangle^+_{nws}$ and (*d*) $\mathrm{d}U^+_{nws}/\mathrm{d}y^+$.

near-wall part of WASS, which account for 5–7 % of the area of the x–z plane. Below $y^+ = 30$, the magnitude of A_{nws}/A_{xz} is larger than that for the no-slip case, in particular, 74.3 % larger near the wall. The streamwise slip induces long tails, observed from the conditional two-point correlations (figure 10*a*). Similar results were reported from the footprints of large-scale motions by a streamwise slip (Yoon *et al.* 2016*b*). As shown in figure 11(*b*), the magnitude of $\langle uu\rangle^+_{nws}$ is larger than that for the no-slip case below $y^+ = 30$, which indicates that the near-wall part of WASS is strengthened by the streamwise slip.

In contrast to $\langle uu\rangle^+_{nws}$, profiles of $\langle -uv\rangle^+_{nws}$ for both cases collapse (figure 11*c*), similar to $\langle -uv\rangle^+$ (figure 2*a*). The streamwise slip results in the enhancement of negative u_{nws} and the attenuation of v_{nws} from the weighted JPDF of $u^+_{nws}v^+_{nws}$ (not shown here). Accordingly, the magnitudes $\langle -uv\rangle^+_{nws}$ for both cases are similar. The near-wall part of WASS contributes to approximately 30 % of the total $\langle -uv\rangle$ despite of a small A_{nws}/A_{xz} (figure 11*c*), representing that they are the main energy-containing motions near the wall. Figure 11(*d*) shows the mean shear ($\mathrm{d}U^+_{nws}/\mathrm{d}y^+$) carried by the near-wall part of WASS. Below $y^+ = 20$, the magnitude of $\mathrm{d}U^+_{nws}/\mathrm{d}y^+$ is larger than that for the no-slip case, especially by 9 % in the vicinity of the wall. The magnitude of $\mathrm{d}U^+_{nws}/\mathrm{d}y^+$ at the wall can be interpreted as the ratio $\tau_{w,nws}/\tau_w$, where $\tau_{w,nws}$ is the wall shear stress carried by the near-wall part of WASS. Given that the wall shear stress is related to the skin friction coefficient, the high $\mathrm{d}U^+_{nws}/\mathrm{d}y^+$ at the wall is responsible for the frictional drag. The majority of discrepancy in $\mathrm{d}U^+_{nws}/\mathrm{d}y^+$ comes from the high A_{nws}/A_{xz} (figure 11*a*). The mean shear of the near-wall part of WASS for the slip case is restored above $y^+ = 30$. In contrast to the upper part of WASS, the near-wall part of WASS can be varied by the viscosity and wall conditions, but their contributions to the streamwise Reynolds stress and Reynolds shear stress are more significant.

Two velocity–vorticity correlations ($\langle v\omega_z\rangle_{nws}$ and $\langle -w\omega_y\rangle_{nws}$) carried by the near-wall part of WASS are plotted in figure 12(*a*,*c*). The former is related to the advective vorticity transport, and the latter represents the vortex stretching (Tennekes & Lumley 1972).

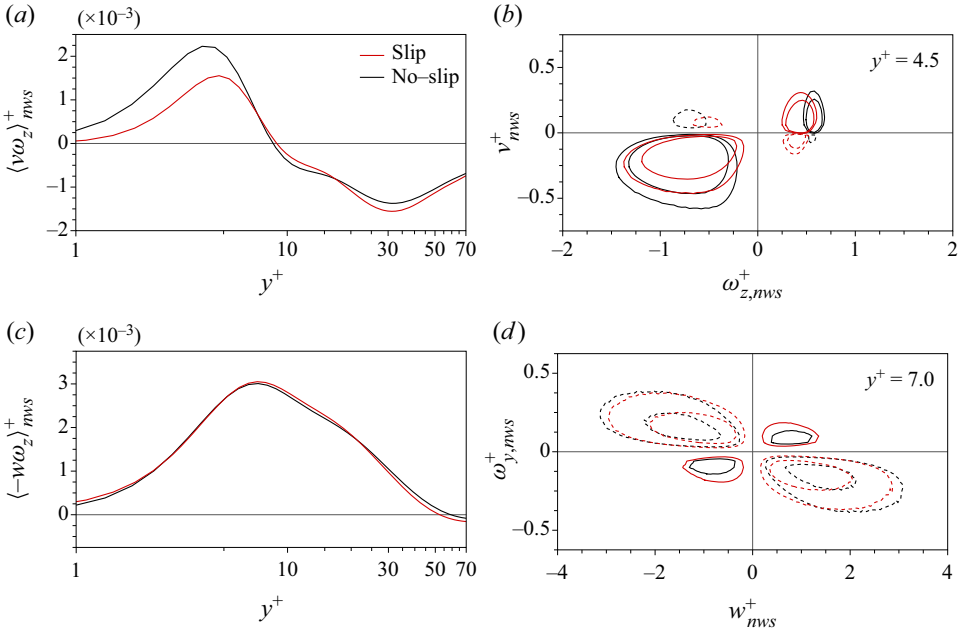

Figure 12. Profiles of velocity–vorticity correlations carried by near-wall part of WASS: (*a*) $\langle v\omega_z\rangle^+_{nws}$ and (*c*) $\langle -w\omega_y\rangle^+_{nws}$. Weighted JPDF of (*b*) $v^+_{nws}\omega^+_{z,nws}$ at $y^+ = 4.5$ and (*d*) $w^+_{nws}\omega^+_{y,nws}$ at $y^+ = 7.0$. The solid and dashed lines correspond to positive and negative values, respectively. Contours are from -0.002 to $+0.002$ with increments of 0.001.

Here, ω_z and ω_y are the spanwise and wall-normal vorticity fluctuations, respectively. In addition, these velocity–vorticity correlations are important to near-wall turbulence, since they are directly related to the frictional drag (Yoon *et al.* 2016*a*; Hwang & Sung 2017; Yoon, Hwang & Sung 2018). The magnitude of $\langle v\omega_z\rangle^+_{nws}$ is significantly reduced near the positive peak at $y^+ = 4.5$ (figure 12*a*). Figure 12(*b*) shows the weighted JPDF of $v^+_{nws}\omega^+_{z,nws}$ at $y^+ = 4.5$, where $\langle v\omega_z\rangle^+_{nws}$ has a positive peak (figure 12*a*). At the first quadrant ($v_{nws} > 0$ & $\omega_{z,nws} > 0$), the magnitude of mean $\omega^+_{z,nws}$ is 28.2 % smaller than that for the no-slip case, and the magnitude of mean v^+_{nws} decreases by 18.4 %. The first quadrant of the weighted JPDF of $v\omega_z$ at a positive peak of $\langle v\omega_z\rangle$ is interpreted as the vertical advection of sublayer streaks (Klewicki, Murray & Falco 1994; Chin *et al.* 2014). Both the weakened near-wall part of WASS and upward motions lead to the reduction in positive $\langle v\omega_z\rangle^+_{nws}$. In addition, a peak is evident in the negative $\langle v\omega_z\rangle^+_{nws}$ at $y^+ = 30$, whereas a negative peak of $\langle v\omega_z\rangle^+$ is observed at $y^+ = 18$ (not shown here), corresponding to outward motions of hairpin vortex heads (Klewicki *et al.* 1994; Chin *et al.* 2014). Given that vortical structures are in the form surrounding streaky structures (Adrian, Meinhart & Tomkins 2000; Lee & Sung 2009; Dennis & Nickels 2011), the conditional field for the near-wall part of WASS does not fully form hairpin-like vortical structures.

Figure 12(*c*) shows wall-normal profiles of $\langle -w\omega_y\rangle^+_{nws}$, in which a positive peak is evident at $y^+ = 7$ and positive values are present up to $y^+ = 50$. The positive $\langle -w\omega_y\rangle$ are physically related to the simultaneous collapse of two adjacent hairpin vortex legs, leading to the stretching of hairpin vortices (Eyink 2008; Chin *et al.* 2014). The magnitude of $\langle -w\omega_y\rangle^+_{nws}$ is similar to that for the no-slip case. Figure 12(*d*) represents the weighted JPDF of $w^+_{nws}\omega^+_{y,nws}$ at $y^+ = 7$, where two motions with negative correlations ($w_{nws} > 0$ and $\omega_{y,nws} < 0$, and $w_{nws} < 0$ and $\omega_{y,nws} > 0$) are dominant. Although the magnitudes of mean

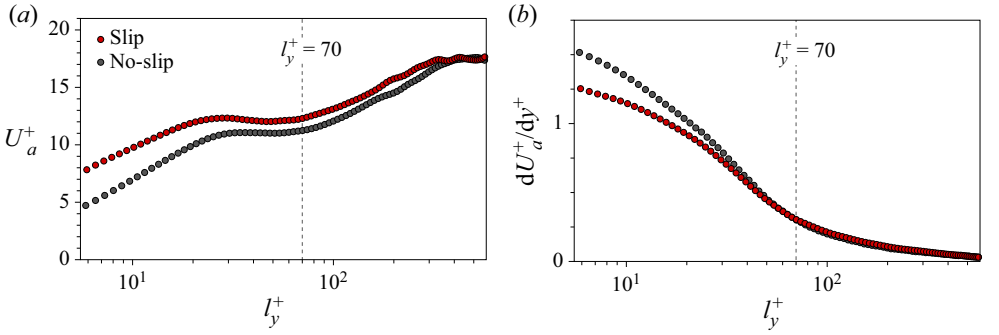

Figure 13. Profiles of (*a*) the convection velocity (U_a^+) and (*b*) the mean shear ($\mathrm{d}U_a^+/\mathrm{d}y^+$) carried by wall-attached structures.

w_{nws}^+ and mean $\omega_{y,nws}^+$ at negative correlations are 25 % and 13 % smaller than those for the no-slip case, the magnitude of $\langle -w\omega_y \rangle^+$ at $y^+ = 7$ is similar to each other due to higher population density of negative correlations. The energy transfer via vortex stretching of the near-wall part of WASS is attenuated by the streamwise slip.

To determine the turbulence statistics reconstructed by the wall-attached structures at a given height, the streamwise velocity and its wall-normal gradient are conditionally averaged as a function of l_y,

$$U_a(l_y) = \left\langle V_a(l_y)^{-1} \int_{V_a} \tilde{u}(\boldsymbol{x})\, \mathrm{d}\boldsymbol{x} \right\rangle, \tag{4.5}$$

$$\frac{\mathrm{d}U_a}{\mathrm{d}y}(l_y) = \left\langle V_a(l_y)^{-1} \int_{V_a} \frac{\mathrm{d}\tilde{u}(\boldsymbol{x})}{\mathrm{d}y}\, \mathrm{d}\boldsymbol{x} \right\rangle. \tag{4.6}$$

Figure 13(*a*) shows the variation in U_a^+ with l_y^+, i.e. the convection velocity of wall-attached structures at a given l_y. A large difference in U_a^+ is observed at $l_y^+ < 30$, while the magnitude of U_a^+ is similar in the region of $l_y^+ \geq 0.45\delta^+$. The discrepancy in U_a^+ at lower l_y^+ is mainly due to the slip velocity at the wall. Interestingly, the difference in U_a^+ decreases as l_y^+ increases. The wall-attached structures slide in the streamwise direction, leading to the increase in their volume close to the wall (figure 10*a*). As l_y^+ increases, the convection velocity of wall-attached structures gets close to that for the no-slip case.

The mean shear ($\mathrm{d}U_a^+/\mathrm{d}y^+$) carried by the wall-attached structures at a given l_y is shown in figure 13(*b*); it is suppressed in the region of $l_y^+ < 50$. Given that the mean shear is directly related to the formation of near-wall streaks (Waleffe 1997), the weakened mean shear results in a lower population density of WABS for the slip case (figure 6*a*). However, profiles of $\mathrm{d}U_a^+/\mathrm{d}y^+$ for both cases collapse well over $l_y^+ < 70$, while the lower population of WASS is observed for the slip case, as shown in figure 6(*a*). This inconsistency reveals that the formation of WASS is affected by the population of WABS (not by the mean shear), supporting the hierarchical distributions of wall-attached structures (Perry & Chong 1982).

To explore the characteristics of the near-wall part of WASS with respect to their height at the near-wall region, conditional averages of wall-parallel area, streamwise velocity, streamwise Reynolds stress and Reynolds shear stress at $y^+ = 14.5$ are examined, which

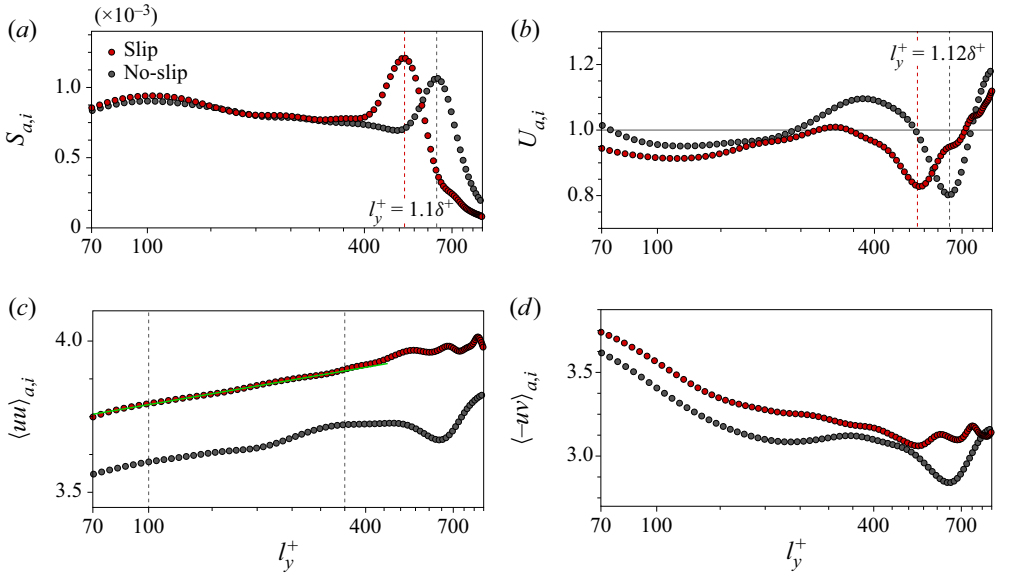

Figure 14. Conditional averages of the near-wall part of WASS at $y^+ = 14.5$: (*a*) $S_{a,i}$; (*b*) $U_{a,i}$; (*c*) $\langle uu\rangle_{a,i}$ and (*d*) $\langle -uv\rangle_{a,i}$. Dashed lines in panels (*a*) and (*b*) represent $l_y^+ = 1.1\delta^+$ and $1.12\delta^+$, respectively. A green line in panel (*c*) denotes the logarithmic variation: $\langle uu\rangle_{a,i} = 0.089 \ln l_y^+ + 3.38$.

are defined as

$$S_{a,i}(l_y) = S_a(y, l_y)|_{y^+=14.5}/(mA_{xz}), \tag{4.7}$$

$$U_{a,i}(l_y) = U_a^*(y, l_y)|_{y^+=14.5}/U(y)|_{y^+=14.5}, \tag{4.8}$$

$$\langle uu\rangle_{a,i}(l_y) = \langle uu\rangle_a^*(y, l_y)|_{y^+=14.5}/\langle uu\rangle(y)|_{y^+=14.5}, \tag{4.9}$$

$$\langle -uv\rangle_{a,i}(l_y) = \langle -uv\rangle_a^*(y, l_y)|_{y^+=14.5}/\langle -uv\rangle(y)|_{y^+=14.5}. \tag{4.10}$$

Figure 14(*a*) shows profiles of the areas in the x–z plane ($S_{a,i}$) occupied by the near-wall part of WASS at $y^+ = 14.5$. The magnitude of $S_{a,i}$ gradually decreases as l_y^+ increases with a peak at $l_y^+ = 1.1\delta^+$. The quantities of $U_{a,i}$, $\langle uu\rangle_{a,i}$ and $\langle -uv\rangle_{a,i}$ describe the dependence on the height of the near-wall part of WASS in their contributions to the turbulence statistics (i.e. U, $\langle uu\rangle$ and $\langle -uv\rangle$) at $y^+ = 14.5$. Figure 14(*b*) represents profiles of $U_{a,i}$ with respect to l_y^+, defined as the convection velocity (U_a^*) of the near-wall part of WASS normalized by U^+ at $y^+ = 14.5$. The region of l_y^+, where the magnitude of $U_{a,i}$ is larger than 1, indicates that positive u of the near-wall part of WASS at a given l_y^+ is dominant near $y^+ = 14.5$, and *vice versa*. A peak of $U_{a,i}$ is observed at $l_y^+ = 310$ (slip) and 370 (no-slip), and a concave peak of $U_{a,i}$ is evident at $l_y^+ = 1.12\delta^+$. In particular, the profile of $U_{a,i}$ is shifted downward from that for the no-slip case, especially in the region of $l_y^+ = 300 - \delta^+$. It shows that the population of wall-attached negative-u structures with $l_y^+ \approx \delta^+$ are more dominant than that for the no-slip case. These observations are consistent with the dominance of negative-u large-scale motions in the outer region (Yoon *et al.* 2016*b*).

We now examine the streamwise Reynolds stress ($\langle uu\rangle_{a,i}$) at $y^+ = 14.5$. Figure 14(*c*) shows the variation in $\langle uu\rangle_{a,i}$ with l_y^+. The magnitude of $\langle uu\rangle_{a,i}$ gradually increases with increasing l_y^+. The contributions of the near-wall part of WASS to the streamwise

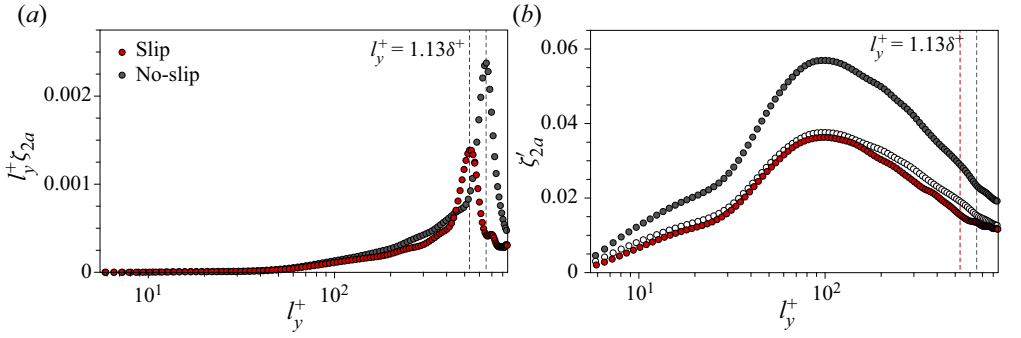

Figure 15. Profiles of (*a*) pre-multiplied ζ_{2a} and (*b*) the density of skin friction (ζ'_{2a}) with respect to l_y^+. Dashed lines represent $l_y^+ = 1.13\delta^+$. Open symbols in panel (*b*) represent $\zeta'_{2a,-34\,\%}$.

Reynolds stress are enhanced as l_y^+ increases. In particular, the magnitude of $\langle uu\rangle_{a,i}$ is logarithmically proportional to l_y^+ in the region of $100 < l_y^+ < 350$ ($\langle uu\rangle_{a,i} \sim \ln l_y^+$) (a green line in figure 15*c*). The inner-peak magnitude of streamwise Reynolds stress logarithmically increases with increasing Re_τ (Jiménez & Hoyas 2008; Marusic, Baars & Hutchins 2017). Since l_y is related to hierarchical scales (figure 7*a*), the logarithmic variation in $\langle uu\rangle_a$ with respect to l_y reflects the hierarchical features of wall-attached structures (Hwang & Sung 2018); this logarithmic variation in $\langle uu\rangle_a$ is evident in the region of $200 < l_y^+ < 300$. A hierarchy of wall-attached structures is well established over the broader range of l_y.

Figure 14(*d*) shows profiles of $\langle -uv\rangle_{a,i}$, of which the value is larger than 3 in the region of $l_y^+ < \delta^+$. It means that the near-wall part of WASS carry three times more Reynolds shear stresses than $\langle -uv\rangle$ in the near-wall region ($y^+ = 14.5$). The magnitude of $\langle -uv\rangle_{a,i}$ is larger than that for the no-slip case below $l_y^+ < \delta^+$. These observations imply that the contributions of the near-wall part of WASS to the near-wall turbulence are dominant, since the Reynolds shear stress is directly related to turbulent contributions to the skin friction coefficient (Fukagata, Iwamoto & Kasagi 2002).

5. Decomposition of C_f

The magnitude of the skin friction coefficient (C_f) is 0.0062 for the no-slip case and 0.0041 for the slip case. Drag reduction can be estimated as $DR = 1 - [1/(1 + \Delta U^+/U_b^+)]^2$ (García-Mayoral *et al.* 2019). The C_f is decomposed into laminar and turbulent components to investigate contributions of wall-attached structures to the frictional drag by using the FIK identity (Fukagata *et al.* 2002) as below:

$$C_f = \frac{2u_\tau^2}{U_b^2} = \underbrace{\frac{6}{Re_b} - \frac{6U_S}{Re_b U_b}}_{=C_{f,1}} + \underbrace{\int_0^1 \frac{6}{U_b^2}(1-y)\langle -uv\rangle \,\mathrm{d}y}_{=C_{f,2}}, \tag{5.1}$$

where $C_{f,1}$ and $C_{f,2}$ are laminar and turbulent terms, respectively. The majority of C_f is produced by $C_{f,2}$; $C_{f,1}$ contributes approximately 10 % of the overall C_f (Yoon *et al.* 2016*b*).

5.1. *Wall-attached structures*

The turbulent term ($C_{f,2}$) can be divided into contributions of wall-attached structures ($C_{f,2a}$) and others ($C_{f,2others}$), which captures contributions of wall-detached structures ($y^+_{min} > 0$) and weak turbulence ($-1.6u_{rms} < u < 1.6u_{rms}$) to $C_{f,2}$. The contribution of wall-attached structures to $C_{f,2}$ can be obtained from the conditional fields:

$$C_{f,2a} = \int_{-\infty}^{\infty} l_y \zeta_{2a}(l_y)\,\mathrm{d}\ln l_y, \quad \text{where } \zeta_{2a}(l_y) = \frac{6}{U_b^2}\left\langle \int_{V_a} -(1-y)u(\boldsymbol{x})v(\boldsymbol{x})\,\mathrm{d}\boldsymbol{x} \right\rangle. \tag{5.2}$$

Here, $l_y\zeta_{2a}$ as a function of l_y is the integrand of $C_{f,2a}$.

Profiles of $l_y^+\zeta_{2a}$ are plotted on a semi-logarithmic scale in figure 15(*a*), where the area of profiles is proportional to $C_{f,2a}$. Those profiles are biased towards higher l_y^+, and peaks are evident at $l_y^+ = 1.13\delta^+$, representing that wall-attached δ-height structures make the dominant contributions to the frictional drag. The area of $l_y^+\zeta_{2a}$ in the region of $l_y^+ \geq 70$ is the same as 97 % of the total area, showing that wall-attached structures with $l_y^+ \geq 70$ are responsible for almost all of the overall $C_{f,2a}$.

To determine the contributions of wall-attached structures at a given l_y to the frictional drag, the density of skin friction (ζ'_{2a}) is defined as

$$\zeta'_{2a}(l_y) = \zeta_{2a}(l_y)\frac{mA_{xz}\delta}{n_a V_a}. \tag{5.3}$$

Figure 15(*b*) shows the profile of ζ'_{2a} with respect to l_y^+. A smooth peak in ζ'_{2a} is evident at $l_y^+ = 100$, which indicates that the wall-attached structures with the height of $l_y^+ \approx 100$ contain the highest density of skin friction. The magnitude of ζ'_{2a} is more than four times larger than C_f beyond $l_y^+ = 30$, in particular, nine times larger near $l_y^+ = 100$. This means that each wall-attached structure is responsible for the generation of turbulent frictional drag (de Giovanetti, Hwang & Choi 2016). Open symbols in figure 15(*b*) represent $\zeta'_{2a,-34\,\%}$. The profile of $\zeta'_{2a,-34\,\%}$ is shifted downward by as much as 34 % from ζ'_{2a}. The magnitude of ζ'_{2a} at $l_y^+ = 1.13\delta^+$ (red dashed line) is similar to that of $\zeta'_{2a,-34\,\%}$ (grey dashed line), representing that the density of skin friction of wall-attached structures with $l_y^+ = 1.13\delta^+$ is similar for both cases. The large difference in $l_y^+\zeta_{2a}$ at $l_y^+ = 1.13\delta^+$ (figure 15*a*) is caused by the volume of wall-attached δ-height structures (figure 6*b*). The magnitude of ζ'_{2a} is 34 % smaller than that of ζ'_{2a} for the no-slip case, especially 44 % in the region of $250 < l_y^+ < 400$.

5.2. *Near-wall part of wall-attached self-similar structures*

To scrutinize contributions of the near-wall part of WASS to the skin friction in detail, the turbulent component of C_f is conditionally averaged as functions of y and l_y,

$$C^*_{f,2a}(y, l_y) = \frac{6}{U_b^2}\left\langle \int_{S_a} -(1-y)u(\boldsymbol{x})v(\boldsymbol{x})\,\mathrm{d}x\,\mathrm{d}z \right\rangle, \tag{5.4}$$

$$C_{f,i}(l_y) = C^*_{f,2a}(y, l_y)|_{y^+=14.5}/C^*_{f,2}(y)|_{y^+=14.5}, \tag{5.5}$$

where $C^*_{f,2}$ is the integrand of $C_{f,2}$ in (5.2) and the double integration of $C^*_{f,2a}$ with respect to y and l_y is the same as $C_{f,2a}$.

Figure 16 shows $C_{f,i}$ with respect to l_y^+, where the area of $C_{f,i}$ is proportional to the contribution of the near-wall part of WASS to $C^*_{f,2}$ at $y^+ = 14.5$. The magnitude

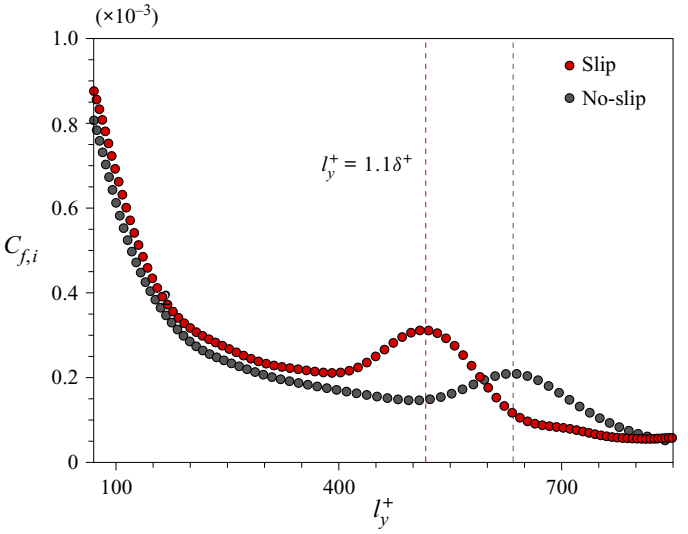

Figure 16. Profiles of pre-multiplied $C_{f,i}$ versus l_y^+. Dashed lines denote $l_y^+ = 1.1\delta^+$.

of $C_{f,i}$ exponentially decreases with the increase in l_y^+. A smooth peak is observed at $l_y^+ = 1.1\delta^+$, where $S_{a,i}$ exhibits a large peak (figure 14*a*). Dominant contributions of the near-wall part of wall-attached δ-height structures to $C_{f,2}$ result from their large area. The contribution of the near-wall part to $C_{f,2}$ in the region of $l_y^+ < 400$ is greater than for the no-slip case, although $S_{a,i}$ is similar below $l_y^+ = 400$ (figure 14*a*). This is due to the enhanced streamwise Reynolds stress and Reynolds shear stress in the vicinity of the wall (figure 14*c*,*d*). The near-wall part of WASS is responsible for 19.1 % of $C^*_{f,2}|_{y^+=14.5}$, which is larger than the no-slip case (17.3 %). Although the near-wall part of WASS occupy only a small area, i.e. approximately 6.3 % of the x–z plane area at $y^+ = 14.5$ (figure 11*a*), its contributions to the skin frictional drag for turbulence are much larger than others.

6. Conclusions

We have explored wall-attached u structures in a drag-reduced turbulent channel flow and demonstrated their contributions to the frictional drag and near-wall turbulence. We extracted 3-D u clusters by using the connectivity of six-orthogonal neighbours in Cartesian coordinates from the DNS dataset for turbulent channel flows with a Navier slip wall ($Re_\tau = 470$) and no-slip wall ($Re_\tau = 577$). We showed that wall-attached structures are formed in their entirety in instantaneous flow fields on the wall with the streamwise slip. The wall-attached structures with the height of $l_y^+ \geq 70 \approx 3Re_\tau^{0.5}$ were self-similar with l_y, and their geometrical features remained unchanged regardless of the streamwise slip. The hierarchical distribution with an inverse power law and the logarithmic behaviour of WASS were also unaffected by the streamwise slip. Influences of the disturbances by the streamwise slip on the wall-attached structures were limited up to the lower bound ($y^+ = 3Re_\tau^{0.5}$) of the logarithmic region. The streamwise slip induced the decrease in the population density of WABS with weakened mean shear. Given that a hierarchy of WASS was sustained, the decrease in the population density of WASS is attributed to that of WABS, whereas the space occupied by WASS in the fluid domain is enlarged. In addition, we focused on the near-wall part ($y^+ < 70$) of WASS ($l_y^+ \geq 70$), and the WABS

($l_y^+ < 70$) were compared. To this end, the conditional average and conditional fields were employed. The near-wall part of WASS was extended in the streamwise direction over 3δ, reminiscent of the footprints of large-scale motions. The near-wall part of WASS contributed to approximately 30 % of the Reynolds shear stress and a quarter of the streamwise Reynolds stress. Next, the skin friction coefficient was decomposed by using the FIK identity to quantify the contributions of wall-attached structures to the frictional drag. The density of skin friction of WASS was more than three-times larger than the magnitude of overall C_f. In addition, the near-wall part of WASS was responsible for approximately 20 % of the turbulent contribution to C_f in the near-wall region despite of the lower volume (5–7 % of total space). The Reynolds shear stress carried by the near-wall part of WASS was enhanced by the streamwise slip, and its contribution to the frictional drag was significant. The streamwise slip curtailed the population density of WASS and the density of skin friction of WASS. The present study enhances our understanding of the behaviour of wall-attached structures and furthers the development of attached-eddy models of drag-reduced flows.

Funding. This work was supported by the National Research Foundation of Korea (NRF) grant funded by the Korea government (MSIT) (No. 2020R1A2C2008106 and 2021R1F1A1053438).

Declaration of interests. The authors report no conflict of interest.

Author ORCIDs.
Min Yoon https://orcid.org/0000-0002-3903-4334;
Hyung Jin Sung https://orcid.org/0000-0002-4671-3626.

References

Adrian, R.J., Meinhart, C.D. & Tomkins, C.D. 2000 Vortex organization in the outer region of the turbulent boundary layer. *J. Fluid Mech.* **422**, 1–54.

Ahn, J., Lee, J.H., Lee, J., Kang, J.H. & Sung, H.J. 2015 Direct numerical simulation of a 30R long turbulent pipe flow at $Re_\tau = 3008$. *Phys. Fluids* **27** (6), 065110.

del Álamo, J.C., Jiménez, J., Zandonade, P. & Moser, R.D. 2006 Self-similar vortex clusters in the turbulent logarithmic region. *J. Fluid Mech.* **561**, 329–358.

Bae, H.J. & Lee, M. 2021 Life cycle of streaks in the buffer layer of wall-bounded turbulence. *Phys. Rev. Fluids* **6** (6), 064603.

Chin, C., Philip, J., Klewicki, J., Ooi, A. & Marusic, I. 2014 Reynolds-number-dependent turbulent inertia and onset of log region in pipe flows. *J. Fluid Mech.* **757**, 747–769.

Chung, D., Monty, J.P. & Ooi, A. 2014 An idealised assessment of Townsend's outer-layer similarity hypothesis for wall turbulence. *J. Fluid Mech.* **742**, R3.

Dennis, D.J. & Nickels, T.B. 2011 Experimental measurement of large-scale three-dimensional structures in a turbulent boundary layer. Part 1. Vortex packets. *J. Fluid Mech.* **673**, 180–217.

Dong, S., Lozano-Durán, A., Sekimoto, A. & Jiménez, J. 2017 Coherent structures in statistically stationary homogeneous shear turbulence. *J. Fluid Mech.* **816**, 167–208.

Eyink, G.L. 2008 Turbulent flow in pipes and channels as cross-stream 'inverse cascades' of vorticity. *Phys. Fluids* **20** (12), 125101.

Flores, O. & Jiménez, J. 2006 Effect of wall-boundary disturbances on turbulent channel flows. *J. Fluid Mech.* **566**, 357–376.

Flores, O., Jiménez, J. & Del Álamo, J.C. 2007 Vorticity organization in the outer layer of turbulent channels with disturbed walls. *J. Fluid Mech.* **591**, 145–154.

Fukagata, K., Iwamoto, K. & Kasagi, N. 2002 Contribution of Reynolds stress distribution to the skin friction in wall-bounded flows. *Phys. Fluids* **14** (11), L73–L76.

Fukagata, K., Kasagi, N. & Koumoutsakos, P. 2006 A theoretical prediction of friction drag reduction in turbulent flow by superhydrophobic surfaces. *Phys. Fluids* **18** (5), 051703.

García-Mayoral, R., Gómez-de-Segura, G. & Fairhall, C.T. 2019 The control of near-wall turbulence through surface texturing. *Fluid Dyn. Res.* **51** (1), 011410.

DE GIOVANETTI, M., HWANG, Y. & CHOI, H. 2016 Skin-friction generation by attached eddies in turbulent channel flow. *J. Fluid Mech.* **808**, 511–538.
HAMILTON, J.M., KIM, J. & WALEFFE, F. 1995 Regeneration mechanisms of near-wall turbulence structures. *J. Fluid Mech.* **287**, 317–348.
HAN, J., HWANG, J., YOON, M., AHN, J. & SUNG, H.J. 2019 Azimuthal organization of large-scale motions in a turbulent minimal pipe flow. *Phys. Fluids* **31** (5), 055113.
HULTMARK, M., VALLIKIVI, M., BAILEY, S.C.C. & SMITS, A.J. 2012 Turbulent pipe flow at extreme Reynolds numbers. *Phys. Rev. Lett.* **108** (9), 094501.
HUTCHINS, N., CHAUHAN, K., MARUSIC, I., MONTY, J. & KLEWICKI, J. 2012 Towards reconciling the large-scale structure of turbulent boundary layers in the atmosphere and laboratory. *Boundary-Layer Meteorol.* **145** (2), 273–306.
HUTCHINS, N. & MARUSIC, I. 2007 Evidence of very long meandering features in the logarithmic region of turbulent boundary layers. *J. Fluid Mech.* **579**, 1–28.
HUTCHINS, N., NICKELS, T.B., MARUSIC, I. & CHONG, M.S. 2009 Hot-wire spatial resolution issues in wall-bounded turbulence. *J. Fluid Mech.* **635**, 103–136.
HWANG, Y. 2015 Statistical structure of self-sustaining attached eddies in turbulent channel flow. *J. Fluid Mech.* **767**, 254–289.
HWANG, J., LEE, J.H. & SUNG, H.J. 2020 Statistical behavior of self-similar structures in canonical wall turbulence. *J. Fluid Mech.* **905**, A6.
HWANG, J., LEE, J., SUNG, H.J. & ZAKI, T.A. 2016 Inner–outer interactions of large-scale structures in turbulent channel flow. *J. Fluid Mech.* **790**, 128–157.
HWANG, J. & SUNG, H.J. 2017 Influence of large-scale motions on the frictional drag in a turbulent boundary layer. *J. Fluid Mech.* **829**, 751–779.
HWANG, J. & SUNG, H.J. 2018 Wall-attached structures of velocity fluctuations in a turbulent boundary layer. *J. Fluid Mech.* **856**, 958–983.
HWANG, J. & SUNG, H.J. 2019 Wall-attached clusters for the logarithmic velocity law in turbulent pipe flow. *Phys. Fluids* **31** (5), 055109.
IBRAHIM, J.I., GÓMEZ-DE-SEGURA, G., CHUNG, D. & GARCÍA-MAYORAL, R. 2021 The smooth-wall-like behaviour of turbulence over drag-altering surfaces: a unifying virtual-origin framework. *J. Fluid Mech.* **915**, A56.
JIMÉNEZ, J. & HOYAS, S. 2008 Turbulent fluctuations above the buffer layer of wall-bounded flows. *J. Fluid Mech.* **611**, 215–236.
KIM, J. 2011 Physics and control of wall turbulence for drag reduction. *Phil. Trans. R. Soc.* A*: Math. Phys. Engng Sci.* **369** (1940), 1396–1411.
KIM, K., BAEK, S.J. & SUNG, H.J. 2002 An implicit velocity decoupling procedure for the incompressible Navier–Stokes equations. *Intl J. Numer. Meth. Fluids* **38** (2), 125–138.
KIM, J., MOIN, P. & MOSER, R. 1987 Turbulence statistics in fully developed channel flow at low Reynolds number. *J. Fluid Mech.* **177**, 133–166.
KLEWICKI, J.C., MURRAY, J.A. & FALCO, R.E. 1994 Vortical motion contributions to stress transport in turbulent boundary layers. *Phys. Fluids* **6** (1), 277–286.
KLINE, S.J., REYNOLDS, W.C., SCHRAUB, F.A. & RUNSTADLER, P.W. 1967 The structure of turbulent boundary layers. *J. Fluid Mech.* **30** (4), 741–773.
LEE, M. & MOSER, R.D. 2015 Direct numerical simulation of turbulent channel flow up to $Re_\tau \approx 5200$. *J. Fluid Mech.* **774**, 395–415.
LEE, J.H. & SUNG, H.J. 2009 Structures in turbulent boundary layers subjected to adverse pressure gradients. *J. Fluid Mech.* **639**, 101–131.
LEE, J.H. & SUNG, H.J. 2013 Comparison of very-large-scale motions of turbulent pipe and boundary layer simulations. *Phys. Fluids* **25** (4), 045103.
LOZANO-DURÁN, A. & BAE, H.J. 2019 Characteristic scales of Townsend's wall-attached eddies. *J. Fluid Mech.* **868**, 698–725.
LOZANO-DURÁN, A., FLORES, O. & JIMÉNEZ, J. 2012 The three-dimensional structure of momentum transfer in turbulent channels. *J. Fluid Mech.* **694**, 100–130.
LOZANO-DURÁN, A. & JIMÉNEZ, J. 2014 Time-resolved evolution of coherent structures in turbulent channels: characterization of eddies and cascades. *J. Fluid Mech.* **759**, 432–471.
MACIEL, Y., GUNGOR, A.G. & SIMENS, M. 2017 Structural differences between small and large momentum-defect turbulent boundary layers. *Intl J. Heat Fluid Flow* **67**, 95–110.
MACIEL, Y., SIMENS, M.P. & GUNGOR, A.G. 2017 Coherent structures in a non-equilibrium large-velocity-defect turbulent boundary layer. *Flow Turbul. Combust.* **98** (1), 1–20.
MARUSIC, I., BAARS, W.J. & HUTCHINS, N. 2017 Scaling of the streamwise turbulence intensity in the context of inner-outer interactions in wall turbulence. *Phys. Rev. Fluids* **2** (10), 100502.

MARUSIC, I. & MONTY, J.P. 2019 Attached eddy model of wall turbulence. *Annu. Rev. Fluid Mech.* **51**, 49–74.

MARUSIC, I., MONTY, J.P., HULTMARK, M. & SMITS, A.J. 2013 On the logarithmic region in wall turbulence. *J. Fluid Mech.* **716**, R3.

MIN, T. & KIM, J. 2004 Effects of hydrophobic surface on skin-friction drag. *Phys. Fluids* **16** (7), L55–L58.

MOISY, F. & JIMÉNEZ, J. 2004 Geometry and clustering of intense structures in isotropic turbulence. *J. Fluid Mech.* **513**, 111–133.

NAVIER, C.L.M.H. 1823 Mémoire sur les lois du mouvement des fluids. *Mém. Acad. R. Sci. Inst. France* **6**, 389–440.

NICKELS, T.B., MARUSIC, I., HAFEZ, S. & CHONG, M.S. 2005 Evidence of the k_1^{-1} law in a high-Reynolds-number turbulent boundary layer. *Phys. Rev. Lett.* **95** (7), 074501.

OSAWA, K. & JIMÉNEZ, J. 2018 Intense structures of different momentum fluxes in turbulent channels. *Phys. Rev. Fluids* **3** (8), 084603.

PERRY, A.E. & ABELL, C.J. 1977 Asymptotic similarity of turbulence structures in smooth-and rough-walled pipes. *J. Fluid Mech.* **79** (4), 785–799.

PERRY, A.E. & CHONG, M.S. 1982 On the mechanism of wall turbulence. *J. Fluid Mech.* **119**, 173–217.

PERRY, A.E., HENBEST, S. & CHONG, M.S. 1986 A theoretical and experimental study of wall turbulence. *J. Fluid Mech.* **165**, 163–199.

RYU, J., BYEON, H., LEE, S.J. & SUNG, H.J. 2019 Flapping dynamics of a flexible plate with Navier slip. *Phys. Fluids* **31** (9), 091901.

TENNEKES, H. & LUMLEY, J.L. 1972 *A First Course in Turbulence*. MIT Press.

TOMKINS, C.D. & ADRIAN, R.J. 2003 Spanwise structure and scale growth in turbulent boundary layers. *J. Fluid Mech.* **490**, 37–74.

TOWNSEND, A.A. 1976 *The Structure of Turbulent Shear Flow*. Cambridge University Press.

WALEFFE, F. 1997 On a self-sustaining process in shear flows. *Phys. Fluids* **9** (4), 883–900.

WANG, L.H., XU, C.X., SUNG, H.J. & HUANG, W.X. 2021 Wall-attached structures over a traveling wavy boundary: turbulent velocity fluctuations. *Phys. Rev. Fluids* **6** (3), 034611.

YANG, J., HWANG, J. & SUNG, H.J. 2019 Influence of wall-attached structures on the boundary of quiescent core region in turbulent pipe flow. *Phys. Rev. Fluids* **4** (11), 114606.

YOON, M., AHN, J., HWANG, J. & SUNG, H.J. 2016*a* Contribution of velocity-vorticity correlations to the frictional drag in wall-bounded turbulent flows. *Phys. Fluids* **28** (8), 081702.

YOON, M., HWANG, J., LEE, J., SUNG, H.J. & KIM, J. 2016*b* Large-scale motions in a turbulent channel flow with the slip boundary condition. *Intl J. Heat Fluid Flow* **61**, 96–107.

YOON, M., HWANG, J. & SUNG, H.J. 2018 Contribution of large-scale motions to the skin friction in a moderate adverse pressure gradient turbulent boundary layer. *J. Fluid Mech.* **848**, 288–311.

YOON, M., HWANG, J., YANG, J. & SUNG, H.J. 2020 Wall-attached structures of streamwise velocity fluctuations in an adverse pressure gradient turbulent boundary layer. *J. Fluid Mech.* **885**, A12.